



Exceptional formaldehyde oxidation at room temperature on Co single-atom functionalized TiO₂ nanowires via highly effective O₂ activation



Lijuan Liu ^a, Guohua Jing ^a, Cibin Xu ^a, Xiaowei Zhang ^a, Xuehong Zhang ^a, Lingyun Guo ^a, Zhiwei Huang ^a, Xiaomin Wu ^a, Huawang Zhao ^a, Chung-Shin Yuan ^b, Huazhen Shen ^{a,*}, Wenjie Xia ^{c,*}

^a College of Chemical Engineering, Huaqiao University, Xiamen, Fujian, China

^b Institute of Environmental Engineering, National Sun Yat-Sen University, No. 70, Lian-Hai Road, Kaohsiung 804, Taiwan

^c Department of Aerospace Engineering, Iowa State University, Ames, IA 50011 USA

ARTICLE INFO

Keywords:

Single atom Co
Titanium dioxide nanowires
Oxygen activation ability
HCHO room temperature oxidation

ABSTRACT

O₂ activation is vital for catalyzing the oxidation of formaldehyde (HCHO). Despite the high O₂ activation capabilities demonstrated by noble metal catalysts, their practical application is impeded by their exorbitant cost. Herein, Co single atoms were successfully incorporated into titanium dioxide nanowires (TiO₂-NWs). Furthermore, the key step in the HCHO catalytic oxidation process was elucidated through *in situ* diffuse reflectance infrared Fourier transform spectroscopy (*in situ* DRIFTS) and density functional theory (DFT) calculations. Finally, the intricate O₂ activation mechanism was explored, revealing the catalyst's exceptional performance in ambient HCHO oxidation. Notably, it outperformed commercial TiO₂ (TiO₂-P25) by 13.3 times and Co-supported TiO₂-P25 by 1.9 times. Co single atoms facilitated the conversion of O₂ into superoxide (O₂[·]), significantly reducing the reaction barrier of dioxymethylene to formate. This superior O₂ activation was attributed to the active nature and unsaturated electronic configuration of Co single atoms. This study provides a novel, cost-effective strategy for creating HCHO elimination catalysts with accessible nonnoble transition metals.

1. Introduction

Formaldehyde (HCHO) is one of the most crucial indoor gaseous pollutants, primarily emanating from the volatilization of urea-formaldehyde resins in indoor building materials, furniture, and decorative products [d1]. Its attributes, including prolonged-release periods and significant toxicity to human health, have spurred growing concern. In 2017, the International Agency for Research on Cancer (IARC) classified HCHO as a class one carcinogen. Studies have demonstrated that even low concentrations of HCHO can cause severe health issues [1]. How to effectively mitigate indoor HCHO levels to protect human health has thus become a matter of widespread concern. Currently, principal technologies for indoor HCHO abatement include adsorption [2,3], photocatalytic oxidation [4,5], low-temperature plasma oxidation [6], and catalytic oxidation (both thermal and nonthermal). Among these, room temperature catalytic oxidation offers a promising way to

efficiently degrade indoor HCHO into H₂O and CO₂ without light or heat excitation [1,7].

Catalytic HCHO oxidation at room temperature produces intermediates such as dioxymethylene (DOM), formate, carbonate, and others, which subsequently decompose into CO₂ and H₂O. However, complete mineralization usually encounters a high reaction barrier, particularly during the conversion of the aldehyde to DOM and the cleavage of C-H bonds within DOM to form formate. These stages often limit the overall reaction rate [8,9].

Reactive oxygen species, specifically superoxide (O₂[·]) generated through O₂ activation, play a crucial role in promoting HCHO and intermediate oxidation [10–12]. Various noble nanoparticles, such as Au, Pt, Pd, and Ag have been explored to enhance O₂ activation, benefiting from the high surface charge density. These metals facilitate electron transfer to O₂, occupying the π^* orbital and reducing O₂ spin [13–16]. However, the scarcity and costliness of precious metals impose practical

* Corresponding authors.

E-mail addresses: hzhsen@hqu.edu.cn (H. Shen), wxia@iastate.edu (W. Xia).

limitations on indoor air purification. Despite significant cost reductions through advancements in single-atom catalysts, their synthesis still causes substantial precious metal losses. We propose utilizing abundant, inexpensive non noble transition metals to prepare single-atom catalysts that activate O₂, enabling highly efficient HCHO catalytic oxidation at room temperature.

Non noble transition metals such as Fe, Co, and Ni, exhibit catalytic activity comparable to Ru, Rh, Pd, and Pt due to similar external d orbital configurations when they are present as single atoms [17–20]. Recently, the activating of O₂ with Co single atoms has attracted significant attention for the selective catalytic oxidation. This activation involves strong O₂ adsorption on Co sites, lengthening the O=O bond. The O₂ adsorption conformation includes end-on adsorption, which evolves into O₂⁺ and releasing less energy, and side-on adsorption, which evolves into peroxide (O₂²⁻) and releasing more energy. Simultaneously, Co single atoms donate electrons to O_{2ad} antibonding 2p orbitals, weakening the O=O bond strength. However, complete O_{2ad} dissociation is much harder with Co single atoms due to the substantially high activation barrier. For instance, Gao et al. [21] calculated a much higher 1.1–1.5 eV activation barrier for Fe single atoms on nitrogen-doped graphene (Fe has comparable O₂ activation to Co). Thus, O₂ or O₂²⁻ actively oxidizes incoming molecules instead of dissociating. Based on this O₂ activation, Co single atoms facilitate various reactions, such as the organosulfur compounds oxidative cleavage and ammonoxidation [22], ethylbenzene oxidation [23], and vegetable oil epoxidation [24].

Herein, we propose a novel approach that utilizes highly dispersed Co single atoms as active centers supported on high specific surface area TiO₂ nanowires (TiO₂-NWs). The strong Co-O interaction leads to O 2p and Co 3d orbital hybridization, facilitating O₂ activation to O₂⁺. This enhancement promotes complete HCHO mineralization. In this study, the Co-O_n coordination was analyzed by aberration-corrected high-angle annular dark field scanning transmission electron microscopy (AC-HAADF-STEM) and X-ray absorption fine structure (XAFS). Subsequently, HCHO catalytic oxidation at room temperature was investigated, and the effects of O₂ and H₂O on the catalytic activity were also explored. Moreover, the decisive step was identified using in situ diffuse reflectance infrared Fourier transform spectroscopy (in situ DRIFTS) and density functional theory (DFT) calculations. Finally, a deep understanding of the O₂ activation mechanism was provided at the molecular level.

2. Experimental methods

2.1. Catalyst preparation

A hydrothermal method was used to prepare the TiO₂-NWs support. A mixture of 1.0 g of commercial TiO₂ (P25) and 10.0 g of NaOH (Sinopharm Group Co. Ltd., Shanghai) was dissolved in 25.0 mL of deionized water (DI H₂O) and stirred for 30 min. The solution was then transferred into a 150 mL Teflon liner and hydrothermally treated at 120 °C for 24 h. The obtained precipitate was washed with diluted HCl (Sinopharm Group Co. Ltd., Shanghai) and DI H₂O to pH = 7.0. Subsequently, the powders were dried overnight at 80 °C and calcined at 400 °C for 2 h in an air atmosphere.

Co/TiO₂-NWs and Co/TiO₂-P25 catalysts were fabricated by impregnation. 1.0 g of TiO₂-NWs were ultrasonically dispersed in 80.0 mL of DI H₂O for 30 min. Then, a 0.01 g/mL aqueous Co(NO₃)₂·6 H₂O (Sinopharm Group Co. Ltd., Shanghai) solution was added dropwise under magnetic stirring at room temperature for 4 h. The precipitates were collected through centrifugation, washed with DI H₂O, and dried overnight at 60 °C. Subsequently, the dried powder was calcined in an air atmosphere at 450 °C for 4 h. Co/TiO₂-P25 was prepared using the same procedures, but TiO₂-P25 was utilized as the support material.

2.2. Catalyst characterization

X-ray diffraction (XRD) analysis was performed using Cu-K α radiation with a Rigaku SmartLab instrument. The specific surface area was determined through N₂ adsorption-desorption experiments, utilizing a Micromeritics ASAP 2460 instrument with the Brunauer–Emmett–Teller (BET) method. Scanning electron microscopy (SEM) was carried out with a ZEISS GeminiSEM 300. High-resolution transmission electron microscopy (HRTEM) images were obtained with a Thermo Fisher Talos F200S instrument. Elemental composition was detected using an Agilent 7700 s inductively coupled plasma optical emission spectrometer (ICP-OES). Ultraviolet-visible diffuse reflectance spectra (UV-Vis) were collected with a Shimadzu UV-3600 instrument. X-ray photoelectron spectroscopy (XPS) analysis was conducted using a Thermo Fisher Escalab 250Xi instrument.

X-ray absorption fine structure (XAFS), including X-ray absorption near-edge structure (XANES) and extended X-ray absorption fine structure (EXAFS), was collected for analyzing the Co K-edge (7709 eV) at the Singapore Synchrotron Light Source (SSL) center. Fluorescence mode was used to record XANES data of the cobalt K-edge, with cobalt foil, Co₃O₄, and CoO serving as references. The storage ring operated at an energy of 2.5 GeV, with an average electron current of less than 200 mA. The acquired EXAFS data were extracted and processed using the IFEFFIT software's ATHENA module as per standard procedures.

O₂ temperature programmed desorption (O₂-TPD) was evaluated using a Quanta chrome instrument. For O₂-TPD, samples were pre-treated by purging with a 30 mL/min He gas flow at 150 °C for 1 h. Then, the samples were cooled to 50 °C and exposed to a 30 mL/min flow of pure O₂ gas for 1 h to achieve O₂ adsorption saturation. Finally, the atmosphere was switched to a high-purity He gas stream (30 mL/min), which was heated to 800 °C for the desorption process at a rate of 10 °C/min under a He atmosphere.

In situ diffuse reflectance infrared Fourier transform spectroscopy (in situ DRIFTS) were acquired using a Thermo Fisher Nicolet iS50 instrument, with samples exposed to an HCHO+N₂+O₂+H₂O stream. Before testing, the catalyst in the in situ reactor underwent a dry N₂ flow at 250 °C for 30 min to clean the surface. It was then cooled to 30 °C to record 4000 to 1000 cm⁻¹ spectra. The resolution was set at 4 cm⁻¹, and they were accumulated over 64 scans, with background spectra subtracted from each one.

2.3. Catalytic activity test

The HCHO oxidation activity of the catalysts (0.17 g) was evaluated in a fixed-bed quartz reactor with a diameter of 6 mm, maintained at 25 ± 2 °C. The catalyst was ground and sieved to a 40–60 mesh before testing. The total feed gas flow rate was 400 mL/min, resulting in a weight hourly space velocity (WHSV) of 140,000 mL/(g·h). The feed gas comprised 10 ppm HCHO, 20 v/v% O₂, H₂O, and N₂ to achieve equilibrium. Gaseous HCHO was generated by purging N₂ into a paraformaldehyde container. The initial HCHO concentration was regulated by adjusting the water bath temperature. Water vapor was generated by purging a N₂ stream through a 40 °C water bubbler. The relative humidity (RH) was controlled by adjusting the N₂ flow rate and monitored by a hygrometer. The HCHO concentration was measured continuously online using an HCHO detector from Interscan (the USA). The CO₂ concentration at the outlet was also continuously analyzed using a flame ionization detector (FID) on a gas chromatograph (FULI GC9790 II).

The HCHO conversion efficiency (%) and CO₂ yield (%) were calculated using the following formulas:

$$\text{HCHO conversion efficiency}(\%) = \left(1 - \frac{[\text{HCHO}]_{\text{out}}}{[\text{HCHO}]_{\text{in}}} \right) \times 100\%$$

$$\text{CO}_2 \text{ yield}(\%) = \frac{[\text{CO}_2]_{\text{out}}}{[\text{HCHO}]_{\text{in}}} \times 100\%$$

where $[HCHO]_{out}$ and $[HCHO]_{in}$ are the HCHO concentrations (ppm) at the outlet and inlet of the reactor, respectively, and $[CO_2]_{out}$ is the CO_2 concentration (ppm) at the outlet.

2.4. DFT method

We conducted all spin-unrestricted density functional theory (DFT) calculations using the Vienna ab initio simulation code. The PBE functional was utilized to simulate the exchange-correlation, while the ion-electron interactions were described using the projector augmented wave (PAW) method. The Hubbard U value was set to 4.20 eV for both Ti and Co [25]. For all periodic structures, the Monkhorst-Pack-grid-mesh-based Brillouin zone k-points were set at $2 \times 2 \times 1$, with a cutoff energy of 450 eV. The convergence criteria for force and energy were set at 0.01 eV/Å and 10^{-5} eV, respectively. Additionally, a 20 Å vacuum layer along the z direction was applied to the surface to mitigate interlayer interference. One anatase TiO_2 slab represented the TiO_2 support, consisting of a $3 \times 2 \times 1$ unit with 108 atoms ($Ti_{36}O_{72}$). The exposed surface was specified as the (101) facet, which is the most thermodynamically stable anatase facet. A single cobalt atom coordinated with four oxygen atoms, consisting of 2 O_{2c} and 2 O_{3c} in the top layer, represented the Co single atom, as shown in Fig. S1.

3. Results and Discussion

3.1. Structural features and coordination states of catalysts

The BET-specific surface areas of TiO_2 -NWs, Co/TiO_2 -NWs, TiO_2 -P25, and Co/TiO_2 -P25 are presented in Table S1. TiO_2 -NWs ($190.2 \text{ m}^2/\text{g}$) have approximately three times the surface area of TiO_2 -P25 ($63.3 \text{ m}^2/\text{g}$). This increased specific surface area facilitates the dispersion of Co species on TiO_2 -NWs, leading to the formation of more active sites [26]. When loading 0.7 wt% Co on TiO_2 -NWs results in a reduction in the specific surface area of Co/TiO_2 -NWs to $108.0 \text{ m}^2/\text{g}$. This decrease is attributed to the partial collapse of nanowire structures during calcination [27].

The crystal structure of each catalyst was investigated by XRD. As seen in Fig. 1a, the XRD peaks of TiO_2 -NWs and TiO_2 -P25 at $2\theta = 25.3^\circ$, 37.8° , 48.1° , 53.9° , 55.1° , 62.7° , 68.9° , 70.3° , 75.1° , and 82.8° correspond to the characteristic peaks of anatase TiO_2 (JCPDS 21-1272). The presence of peaks at $2\theta = 27.4^\circ$, 36.1° , and 41.2° in TiO_2 -P25, in addition to the anatase peaks, indicates the coexistence of two phases: anatase and rutile TiO_2 (JCPDS 34-0180). This suggests that anatase

predominates the crystal phase of TiO_2 -NWs, whereas TiO_2 -P25 has a mixture of anatase and rutile. Upon loading with Co species, both Co/TiO_2 -NWs and Co/TiO_2 -P25 maintain their original crystalline phase. Notably, the XRD spectra of Co/TiO_2 -NWs and Co/TiO_2 -P25 do not show characteristic peaks of CoO (42.4° and 34.2°), Co_3O_4 (46.9°), or metallic Co species (44.2° and 47.6°). This phenomenon may arise from the low Co species content, which falls below the detection limit.

The UV-Vis diffuse reflection spectra demonstrates the successful loading of Co^{2+} on TiO_2 -NWs and TiO_2 -P25. As shown in Fig. 1b, Co/TiO_2 -NWs and Co/TiO_2 -P25 exhibit substantial absorption within the visible region (400–700 nm). The absorption region spanning from 420 to 520 nm (indicated by a rectangle) corresponds to the 4T_1g -to- $^4T_1g(p)$ transition of Co^{2+} , while a weaker peak (marked by an arrow) at 680 nm is ascribed to the 4T_1g -to- 4A_2g transition induced by high-spin $Co^{2+}(3d^7)$ [28,29]. In contrast, TiO_2 -NWs and TiO_2 -P25 display minimal optical response in the visible-light region.

The electronic states of Ti and O elements were characterized by XPS. Fig. 2a shows the high-resolution XPS spectra of Ti 2p for the catalysts. Compared to TiO_2 -P25, TiO_2 -NWs exhibit a negative shift in both $Ti 2p_{1/2}$ and $Ti 2p_{3/2}$ peaks, indicating increased oxygen vacancies and Ti^{3+} in TiO_2 -NWs [30,31]. After Co loading, the Ti 2p binding energy for Co/TiO_2 -NWs and Co/TiO_2 -P25 also shifts to lower energy relative to their supports, implying that more Ti^{4+} is chemically reduced. This reduction arises from strong Co-O interactions, weakening the Ti-O bonds and increasing the electron cloud density around Ti species [32]. Consequently, for maintaining charge balance, more oxygen vacancies are generated on Co/TiO_2 -NWs and Co/TiO_2 -P25. In Fig. 2b, the dominant peak at approximately 529.5 eV corresponds to lattice oxygen (O_L) in the support. Peaks at approximately 531.0 eV are attributed to surface chemisorbed oxygen (O_S), while higher binding energy peaks ranging from 532 to 533 eV are associated with surface hydroxyl oxygen (O_H) of Ti-OH [33]. Table 1 summarizes the ratios of these oxygen species, with the order of O_S concentration as Co/TiO_2 -NWs > Co/TiO_2 -P25 > TiO_2 -NWs > TiO_2 -P25. This indicates that TiO_2 -NWs have more active oxygen species than TiO_2 -P25 due to their abundant oxygen vacancies [34]. Additionally, the higher number of active oxygen species on Co/TiO_2 -NWs and Co/TiO_2 -P25 versus their supports suggests that Co species induce the formation of more active oxygen [35]. Furthermore, Co/TiO_2 -NWs possess more oxygen species than Co/TiO_2 -P25, suggesting that Co is more effective at generating oxygen species on TiO_2 -NWs than TiO_2 -P25. Notably, the O_L 1s peaks of Co/TiO_2 -NWs and Co/TiO_2 -P25 also shift negatively after Co loading, meaning strong Co-O interactions that draw the electron cloud from Co to neighboring O_L [36]. The presence of O_H peaks in TiO_2 -NWs, Co/TiO_2 -NWs, and Co/TiO_2 -P25 is attributed to H_2O activation by

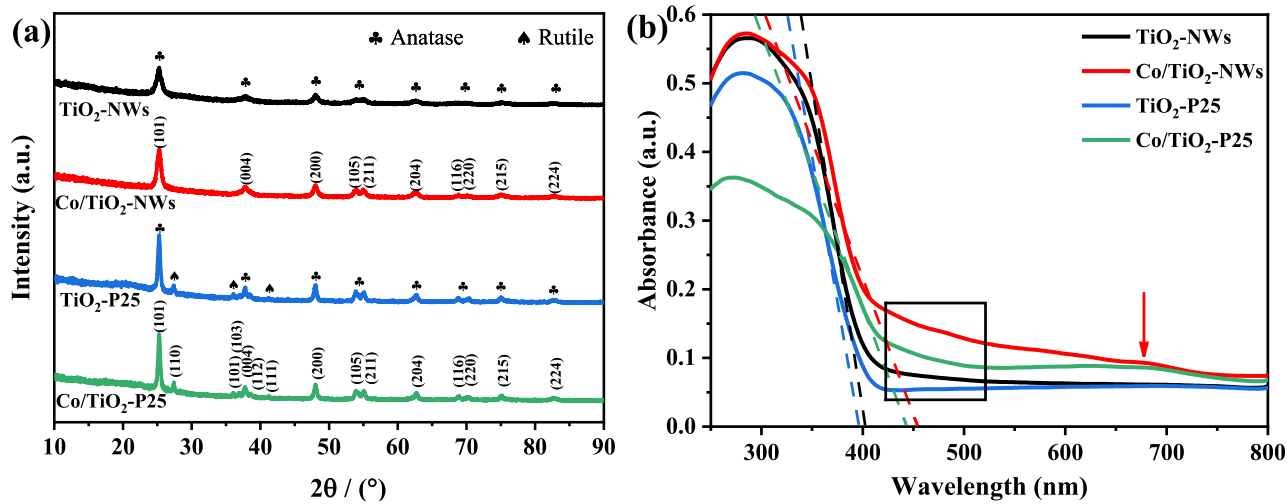


Fig. 1. (a) XRD patterns and (b) UV-Vis diffuse reflectance spectra of TiO_2 -NWs, Co/TiO_2 -NWs, TiO_2 -P25 and Co/TiO_2 -P25.

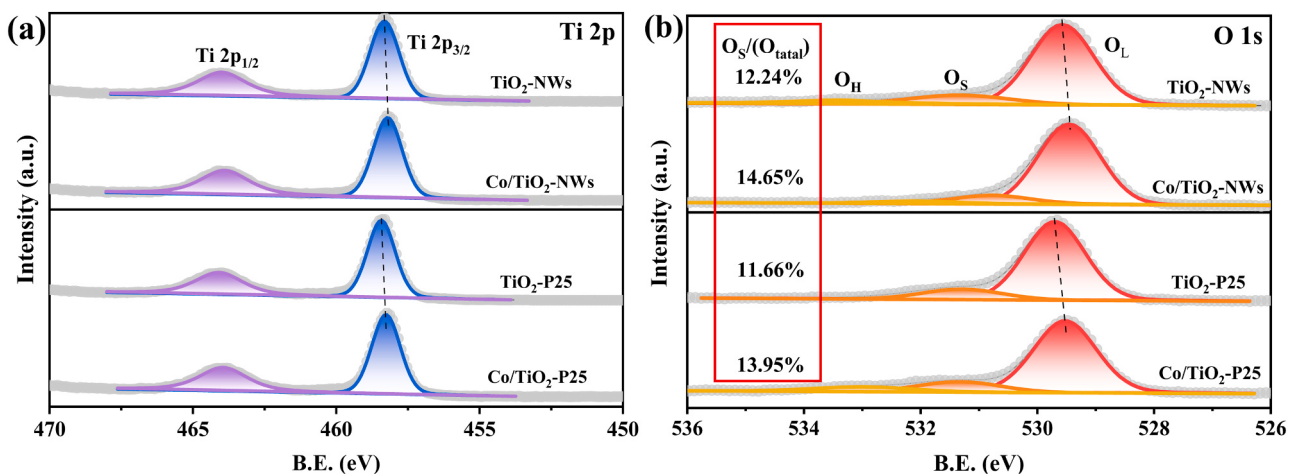


Fig. 2. XPS spectra of (a) Ti 2p and (b) O 1s for TiO_2 -NWs, Co/TiO_2 -NWs, TiO_2 -P25 and Co/TiO_2 -P25.

Table 1

XPS peaks of Ti 2p, O 1s for TiO_2 -NWs, Co/TiO_2 -NWs, TiO_2 -P25, and Co/TiO_2 -P25.

Catalyst	TiO_2 -NWs	Co/TiO_2 -NWs	TiO_2 -P25	Co/TiO_2 -P25
BE of $\text{Ti} 2\text{p}_{3/2}$ (eV)	458.32	458.20	458.43	458.26
BE of $\text{O}_1 \text{s}_{1/2}$ (eV)	529.57	529.46	529.70	529.53
$\text{O}_s/\text{O}_{\text{total}}$ (%)	12.24	14.65	11.66	13.95

active oxygen generated through oxygen vacancies, leading to hydroxyl group (-OH) formation [37]. Additionally, the higher surface -OH ratio for Co/TiO_2 -NWs and Co/TiO_2 -P25 versus their respective support arises from more oxygen vacancies on the Co-loaded TiO_2 .

SEM, HRTEM, and AC-HAADF-STEM were employed to examine the distribution of Co species on TiO_2 -NWs and TiO_2 -P25. The distinctive “wire” structure evident in Figs. 3a-3c verifies the successful morphological construction of TiO_2 -NWs and Co/TiO_2 -NWs. In addition, the spacing between lattice stripes in Co/TiO_2 -NWs measures approximately 0.35 nm, corresponding to the (101) facet of anatase TiO_2 . Although HRTEM does not directly reveal the lattice fringe of Co-containing species such as Co metal, CoO , and Co_3O_4 in Co/TiO_2 -NWs. As shown in Fig. 3d, bright spots (highlighted within the red circle) are discernible in the AC-HAADF-STEM image. Additionally, the EDS mapping image of Co/TiO_2 -NWs in Fig. 3e distinctly displays the highly dispersed Co elements. Hence, the Co-containing species are confirmed to exist as single atoms highly dispersed on TiO_2 -NWs [38]. In contrast, the nanogranular morphology evident in Figs. 3f and 3g for TiO_2 -P25 and Co/TiO_2 -P25, respectively, is distinct from that of TiO_2 -NWs and Co/TiO_2 -NWs. Notably, a distinct lattice stripe with an average spacing of 0.21 nm, corresponding to the $\text{CoO}(200)$ crystal facet [39], is discerned in Fig. 3h. The EDS analysis further confirms the distribution of CoO nanoparticles on the surface of Co/TiO_2 -P25 in Fig. 3i. Consequently, TiO_2 -NWs, with a larger specific surface area, facilitate the monoatomic dispersion of individual Co atoms, while Co species manifest as CoO nanoparticles on TiO_2 -P25.

XAFS was applied to ascertain the valence state and chemical coordination environment of Co on Co/TiO_2 -NWs. Fig. 4a shows that the rising edge of Co/TiO_2 -NWs closely coincides with that of CoO in the XANES spectrum of the Co K-edge, revealing that Co atoms within Co/TiO_2 -NWs predominantly exist in a +2 valence state [33]. In the FT-EXAFS spectrum of Co/TiO_2 -NWs (Fig. 4b), the primary peak appears at 1.93 Å, corresponding to the nearest backscattering path of Co-O [40]. This distance differs from CoO (1.99 Å) and Co_3O_4 (1.75 Å), implying a distinct coordination environment for Co atoms in Co/TiO_2 -NWs compared to CoO and Co_3O_4 . Furthermore, Fig. 4b shows

the absence of the main peak at 2.45 Å, attributed to the Co-Co bond in Co foil [41], in the Co/TiO_2 -NWs spectrum. This absence indicates that no metallic Co exists in Co/TiO_2 -NWs. Combined with the AC-HAADF-STEM results, these results confirm the presence of monoatomic Co in Co/TiO_2 -NWs.

As a result of achieving dispersion of Co single atoms through the impregnation method, these Co atoms preferentially attach to interstitial sites rather than substituting surface Ti atoms. The HRTEM image confirms that the exposed (101) facet of Co/TiO_2 -NWs, known for its high thermal stability in anatase TiO_2 , serves as the supporting structure for anchoring Co single atoms. As such, the interstitial site enclosed by four surface oxygen atoms ($\text{Co}-\text{O}_4$) on the sawtooth-like (101) facet is identified as the most favorable anchoring site of Co single atoms, as confirmed by DFT calculations (Fig. 4c). The average distance between the isolated Co atom and the four bonded O atoms (1.94 Å), between the Co atom and four surrounding Ti atoms (2.65 Å), and between the Co atom and the nonbonded O atom (3.14 Å) align with the three peak positions observed in the FT-EXAFS of Co/TiO_2 -NWs. This established structure was further utilized to fit the experimental FT-EXAFS spectrum of Co/TiO_2 -NWs, as depicted in Fig. 4d and S2. The simulated bond length of 1.95 Å corresponding to the Co-O bond concurs well with the experimental primary peak, reinforcing that the Co single atom forms covalent bonds with four oxygen atoms. Detailed fitting parameters are shown in Table S2. Wavelet transform (WT) analysis was applied to identify the backscattering atoms and provide powerful resolution in both R and k spaces. Figs. 4e-4h portray the WT contour plot of Co/TiO_2 -NWs exhibiting a maximum intensity adjacent to 3.70 Å⁻¹, closely resembling the maximum intensities of CoO (3.91 Å⁻¹) and Co_3O_4 (3.54 Å⁻¹). This observation validates that the intensity of Co/TiO_2 -NWs corresponds to backscattering between Co and O atoms [42]. Additionally, the absence of a maximum intensity corresponding to Co-Co coordination at approximately 6.78 Å⁻¹ in Co/TiO_2 -NWs, as observed in Co foils, confirms that Co atoms in Co/TiO_2 -NWs exist as single atoms.

3.2. Catalytic activity in HCHO conversion

As shown in Figs S3 and S4, the catalytic activity of TiO_2 -NWs is quite low, initiating with an approximately 20% conversion efficiency and gradually decreasing within 90 min. However, Co/TiO_2 -NWs exhibit a notably improved conversion efficiency and reaction rate of HCHO with increased Co content, reaching the highest efficiency with 0.7 wt% Co/ TiO_2 -NWs. This phenomenon arises because lower Co concentrations induce fewer active sites, while higher Co loadings tend to generate CoO_x nanoparticles with reduced atom utilization, decreasing catalytic activity. Consequently, Co/TiO_2 -NWs with the optimal 0.7 wt% Co content demonstrate remarkable HCHO conversion efficiency, achieving

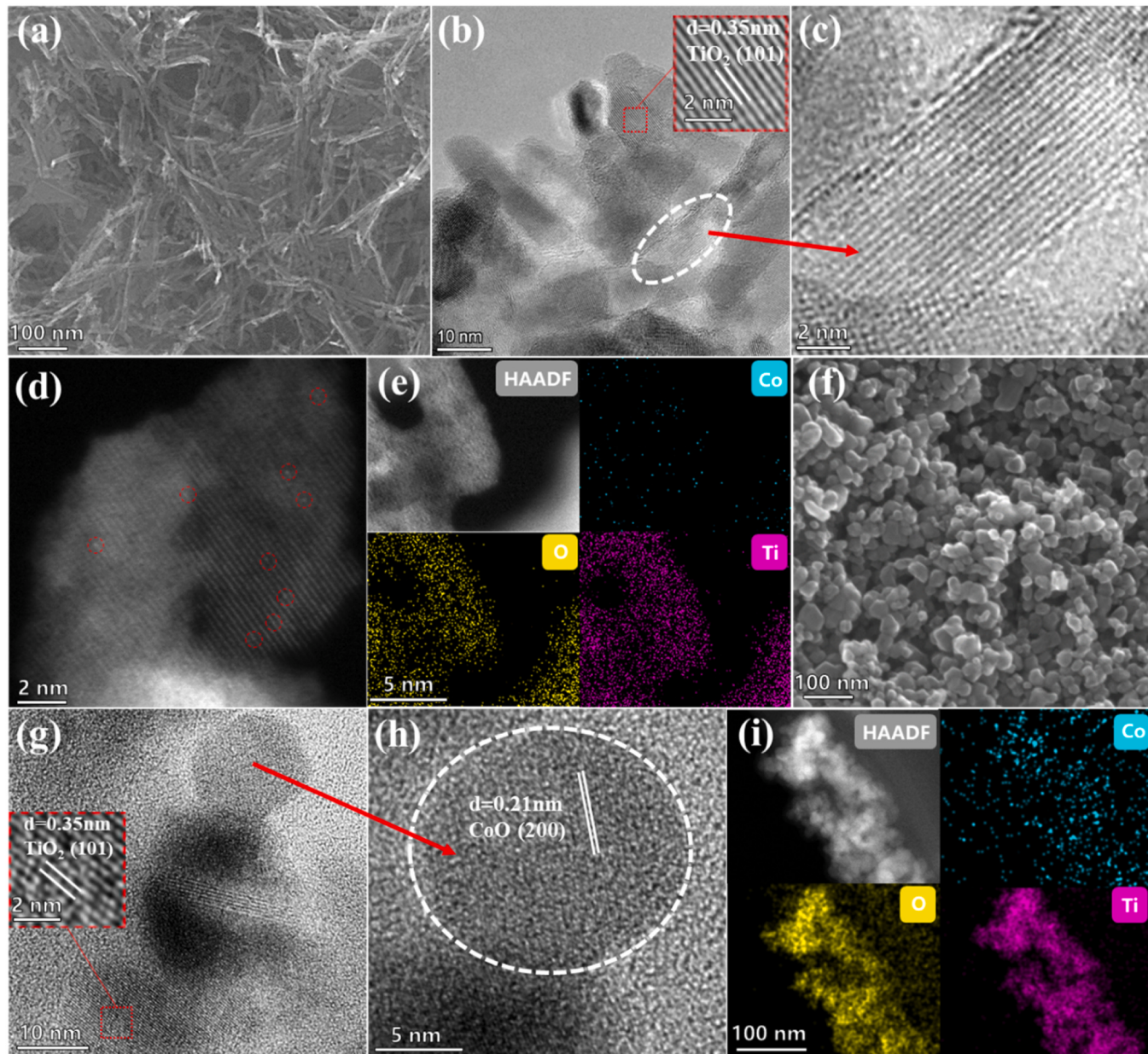


Fig. 3. (a) SEM image of TiO_2 -NWs, (b)-(c) HRTEM image, (d) AC-HAADF-STEM image and (e) EDS mapping images of Co/TiO_2 -NWs, (f) SEM image of TiO_2 -P25, (g)-(h) HRTEM images and (i) EDS mapping images of Co/TiO_2 -P25.

nearly 100% and maintaining it over 4 h (Figs. 5a and 5b). In contrast, none of the other catalysts sustain high stable activity throughout the test, particularly TiO_2 -NWs and TiO_2 -P25, where conversion efficiencies drop below 30%. Accordingly, the CO_2 yield of these catalysts follows a similar trend (Fig. 5c), with Co/TiO_2 -NWs outperforming all others and achieving a high 98.3% CO_2 yield. In contrast, TiO_2 -NWs and TiO_2 -P25 exhibit considerably lower CO_2 yields, remaining below 20% within the short measurement period. Furthermore, Co/TiO_2 -P25 (0.7 wt% Co) also underperforms compared to Co/TiO_2 -NWs, showing a continuous decline in CO_2 yield. To exclude the influence of specific surface area, Fig. S5 shows the reaction rate per specific surface area (R_s) at room temperature. Notably, the R_s of Co/TiO_2 -NWs is 9.2, 5.7, and 1.5 times higher than that of TiO_2 -NWs, TiO_2 -P25, and Co/TiO_2 -P25, respectively. These results confirm that Co single atoms most effectively enhance the catalytic activity of TiO_2 for HCHO oxidation. Additionally, we conducted a comprehensive overview of the documented catalytic activity of Co-based catalysts (as shown in Table S3 and Fig. S6). We also

evaluated Pt/TiO_2 [43] and $\sigma\text{-MnO}_2$ [44] for HCHO degradation under identical conditions (Figs. S7 and S8). Through comparison, it is evident that Co/TiO_2 -NWs exhibit exceptional catalytic activity for HCHO decomposition.

To investigate the impact of O_2 on HCHO conversion, we examined the HCHO conversion efficiency of Co/TiO_2 -NWs in the presence and absence of O_2 . Fig. 5d illustrates that the absence of O_2 significantly decreases the CO_2 yield, highlighting the crucial role of O_2 in the catalytic oxidation of HCHO. However, even without O_2 , Co/TiO_2 -NWs still retain 33.8% catalytic activity, implying an alternative reaction pathway in the absence of O_2 , possibly involving peroxygen formation due to the activation of adsorbed O_2 by oxygen vacancies [45].

In addition, the catalytic behavior of Co/TiO_2 -NWs under different WHSV conditions was measured (Fig. S9). At low WHSVs of 70000 and 140000 mL/(g·h), O_2 and HCHO have a relatively long residence time on the catalyst surface, leading to higher HCHO conversion. Conversely, at a high WHSV of 210000 mL/(g·h), inadequate surface residence time

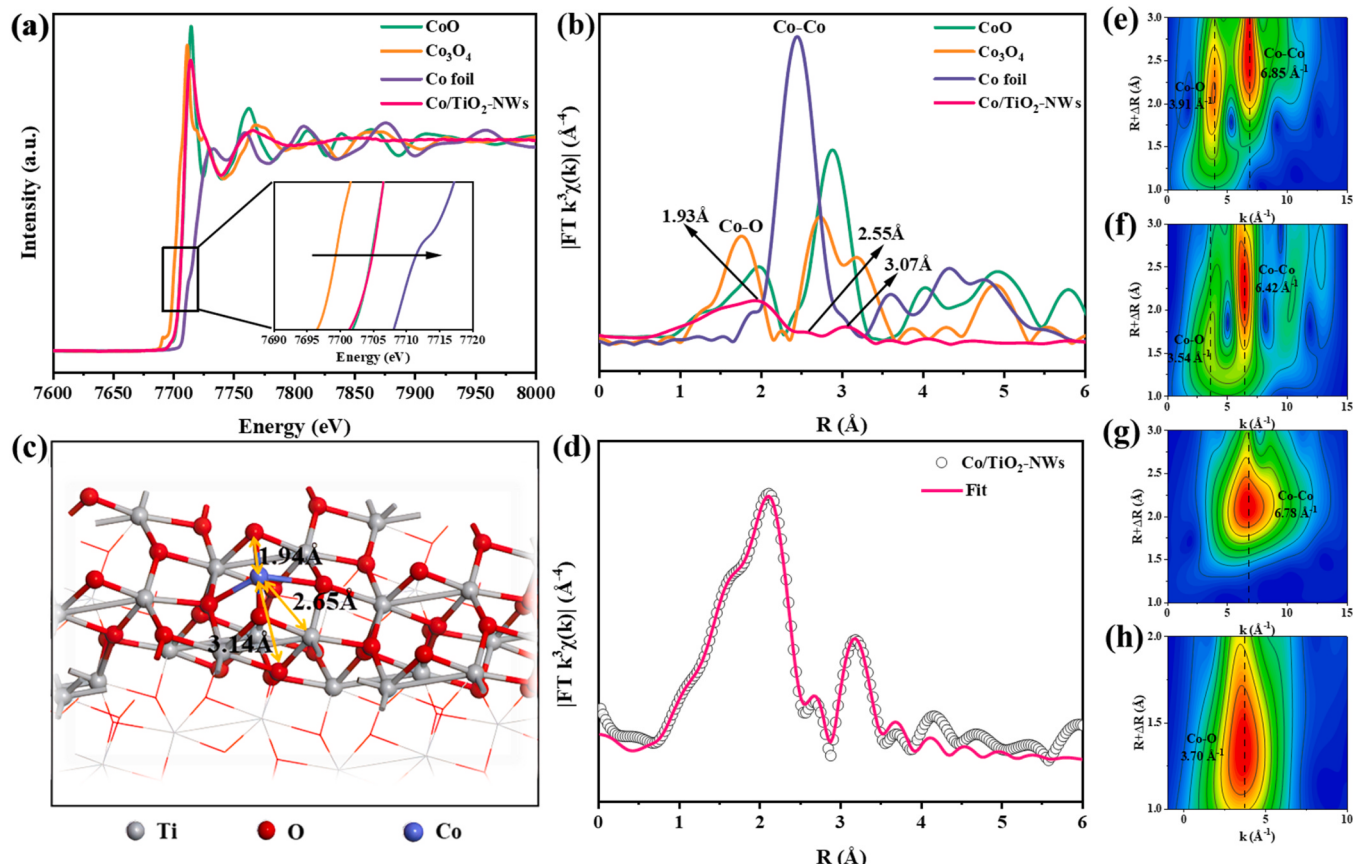


Fig. 4. (a) Normalized Co K-edge XANES spectra of Co foil, Co_3O_4 , CoO , and Co/TiO_2 -NWs, (b) Co K-edge FT-EXAFS spectra for Co/TiO_2 -NWs and reference samples, (c) DFT model of Co/TiO_2 -NWs, (d) FT-EXAFS fitting of Co/TiO_2 -NWs, (e)-(h) Co K-edge WT-EXAFS contour plots for CoO , Co_3O_4 , Co foil, and Co/TiO_2 -NWs.

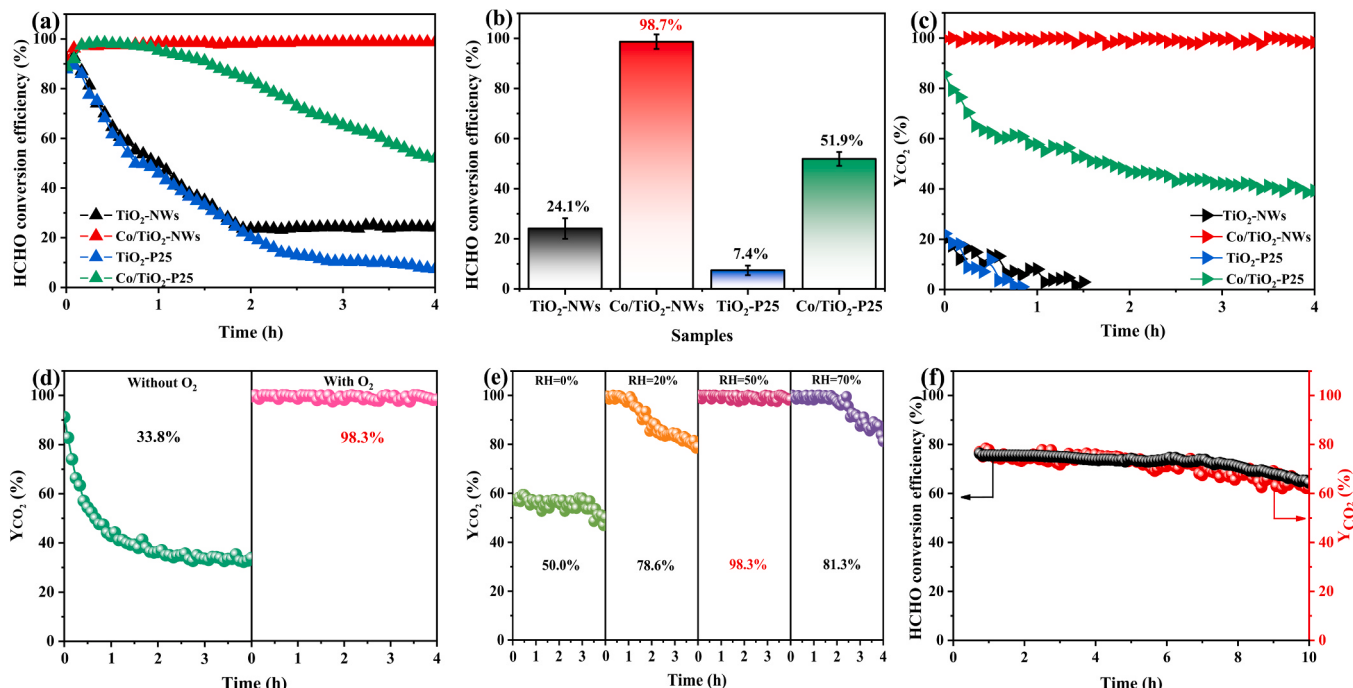


Fig. 5. (a) (b) HCHO conversion efficiency and (c) CO_2 yields of TiO_2 -NWs, Co/TiO_2 -NWs, TiO_2 -P25 and Co/TiO_2 -P25, (d) CO_2 yields of Co/TiO_2 -NWs in the presence and absence of O_2 , (e) CO_2 yields of Co/TiO_2 -NWs under different RH conditions and (f) stability test. Reaction conditions: 10 ppm of HCHO, 20 v/v% O_2 , 50% RH, WHSV = 140,000 mL/(g·h) if not specified.

impedes O₂ activation and HCHO adsorption.

The effect of RH on catalytic HCHO oxidation by Co/TiO₂-NWs was investigated. Fig. 5e shows that even under dry conditions (RH = 0%), Co/TiO₂-NWs exhibit a CO₂ yield of 50.0%. Moreover, the CO₂ yield remains steady for over 4 h during catalytic oxidation, suggesting that surface hydroxyl groups are not gradually depleted. Hence, the surface hydroxyl groups of Co/TiO₂-NWs likely function as HCHO adsorption sites rather than acting as oxidative centers for formate-to-CO₂ oxidation [46]. At 50% RH, Co/TiO₂-NWs demonstrate the most efficient and stable CO₂ yield of 98.3%. However, the CO₂ yield decreases at 30% or 70% RH. This suggests that an appropriate amount of H₂O enhances surface hydroxyl groups because active oxygen atoms can react with single H₂O molecules to form surface hydroxyl groups, as confirmed by DFT calculations (Fig. S10). However, excessive H₂O hampers oxidation efficiency through competitive adsorption with HCHO [47,48]. DFT calculations also demonstrate that the primary competition between H₂O and HCHO primarily occurs at the surface OH group of Co/TiO₂-NWs through a hydrogen bond (E = -0.12 eV) (Fig. S11).

The influence of residual Na⁺ on catalytic activity was investigated due to the use of NaOH in synthesizing the TiO₂-NWs support. Two variants of Co/TiO₂-NWs, containing 0.49 wt% and 1.04 wt% Na⁺, were prepared with different DI H₂O washes after synthesizing Co/TiO₂-NWs. As depicted in Fig. S12, both Co/TiO₂-NWs exhibit similar HCHO oxidation activity despite different Na⁺ contents. Additionally, the Na XPS analysis in Fig. S13 indicates an identical 1072.3 eV Na 1 s binding energy for TiO₂-NWs and Co/TiO₂-NWs, revealing no electron transfer between Na⁺ and Co²⁺ within Co/TiO₂-NWs. Therefore, these results suggest a minimal influence of residual Na⁺ on the overall catalytic performance.

To investigate the stability of the Co/TiO₂-NWs' catalytic activity, we conducted additional tests to evaluate the HCHO conversion efficiency (WHSV=280000 mL/(g·h)) and CO₂ yield (WHSV=175000 mL/(g·h)) over a 10-hour period. Fig. 5f illustrates that Co/TiO₂-NWs initially exhibited a complete CO₂ yield of over 70% within the first 5 h. However, as the reaction proceeded, the catalyst experienced gradual deactivation, ultimately reaching approximately 60% CO₂ yield within the 10-hour period. Nevertheless, high-temperature calcination can restore the deactivated Co/TiO₂-NWs to an excellent catalytic performance (Fig. S14), suggesting the effective removal of accumulated intermediates and the renewal of the active sites.

3.3. Catalytic oxidation mechanism of HCHO

To investigate the role of Co single atoms in the catalytic conversion pathway of HCHO over Co/TiO₂-NWs, we conducted *in situ* DRIFTS measurements at 30 °C on Co/TiO₂-NWs, TiO₂-NWs, and Co/TiO₂-P25 in the presence of HCHO (10 ppm), O₂ (20 v/v%), and H₂O (50% RH). The time-dependent peak intensities for Co/TiO₂-NWs, TiO₂-NWs, and Co/TiO₂-P25 are summarized in Table 2 and visualized in Figs. 6a-6c.

For Co/TiO₂-NWs in Fig. 6a, the peaks at 1175 cm⁻¹ (v_{OCO}), 1445, 1420 cm⁻¹ (δ_{CH₂}), and 1245 cm⁻¹ (v_{CH₂}) corresponding to DOM gradually rise, indicating DOM formation through the active oxygen of Co/TiO₂-NWs interacting with HCHO carbon. Concurrently, peaks at 1602 and 1580 cm⁻¹ (v_{asOCO}), 1370 cm⁻¹ (v_{SOCO}), 2954, 2905, 2862 cm⁻¹ (v_{CH}), and 1393 cm⁻¹ (δ_{CH}) representing monodentate formate emerge. Additionally, bands at 1532 and 1330 cm⁻¹ corresponding to monodentate carbonates on Co/TiO₂-NWs accumulate, indicating formate oxidation into carbonates. The presence of CO₂ peaks at 2322 cm⁻¹ suggests further carbonate decomposition into CO₂. Additionally, the range of 3000–3600 cm⁻¹ (v_{OH}) and the peak at 1647 cm⁻¹ (δ_{CH}) from H₂O are intensified, indicating H₂O as the final catalytic oxidation product of HCHO. Consequently, the catalytic oxidation path over Co/TiO₂-NWs involves DOM formate carboxylate CO₂ + H₂O over Co/TiO₂-NWs [46,61].

For TiO₂-NWs (Fig. 6b), peaks at 1445 cm⁻¹ (v_{CH₂}) corresponding to DOM gradually accumulate. However, peaks at 1565 cm⁻¹ (v_{asOCO}),

Table 2

Characteristic peaks of intermediates during HCHO catalytic oxidation on Co/TiO₂-NWs, TiO₂-NWs, and Co/TiO₂-P25.

Species	Vibrational modes	Catalysts			Refs.
		TiO ₂ -NWs	Co/TiO ₂ -NWs	Co/TiO ₂ -P25	
DOM	δ(CH ₂)	1445, 1420	1475, 1445, 1420	1475, 1420	[49–51]
	v(CH ₂)	1245	1245	1245	[49,50]
	v(OCO)	1175	1175	1175	[46]
	v(CH)	2960, 2901,	2954, 2905,	2960, 2902,	[52–54]
		2842	2862	2862	
	v _{as} (OCO)	1565	1602, 1580	1582	[32], [53–55]
	δ(CH)	1393	1393	1393	[55]
	v _s (OCO)	1370	1370	1360	[53,54], [56,57]
	CO ₃ ²⁻	Monodentate	1532, 1510, 1330	1532, 1510, 1330	[56],[58]
	CO ₂	-	2345	2322	2315
OH ^I	v(OH)	3730	3730	3710	[46]
	OH ^{II}	3697	3690	3680	[46],[59]
	H ₂ O	3000-	3000-	3000-	[46],[59]
		3600	3600	3600	60]
	δ(OH)	1638	1647	1646	

*OH^I: terminal coordinated OH species, OH^{II}: bridging coordinated OH species.

1370 cm⁻¹ (v_{OCO}), 2960, 2901, 2842 cm⁻¹ (v_{CH}), and 1393 cm⁻¹ (δ_{CH}) representing monodentate formate disappear compared to Co/TiO₂-NWs (Fig. 6a). Furthermore, the evolution of formate species over the catalysts within 60 min was compared, as shown in Fig. 6e. The formate species peak intensity at 1393 cm⁻¹ in TiO₂-NWs increases more slowly than that in Co/TiO₂-NWs, implying that DOM's transformation into formate is more difficult for TiO₂-NWs, possibly constituting a rate-determining step. Additionally, the characteristic CO₂ peak only appears after 30 min for TiO₂-NWs, whereas CO₂ is generated within one minute for Co/TiO₂-NWs. Therefore, the different DRIFTS profiles between TiO₂-NWs and Co/TiO₂-NWs suggest that Co single atoms significantly accelerate the catalytic oxidation of HCHO by promoting DOM transformation into formate.

Fig. 6c of Co/TiO₂-P25 was measured to compare the influence of Co single atoms and CoO nanoparticles on the catalytic oxidation of HCHO. The peaks attributed to DOM, formate, carbonate, and CO₂ are also present for Co/TiO₂-P25. Within one minute, a large number of DOM species appear on Co/TiO₂-P25. However, compared with Co/TiO₂-NWs in Fig. 6a, Co/TiO₂-P25's peaks representing monodentate formate at 1582, 1393, and 1360 cm⁻¹ are relatively weak. This suggests that DOM to formate conversion in Co/TiO₂-P25 is less efficient than that in Co/TiO₂-NWs, leading to substantial DOM accumulation. Fig. 6f shows the DOM accumulation comparison on each catalyst within 60 min, revealing extremely low DOM accumulation on Co/TiO₂-NWs. This disparity in DOM conversion between Co/TiO₂-NWs and Co/TiO₂-P25 stems from the varying oxygen activation abilities of Co single atoms and CoO nanoparticles.

To explore the promotional effect of O₂ on HCHO catalytic oxidation, we conducted *in situ* DRIFTS analysis of Co/TiO₂-NWs exposed to HCHO (10 ppm) + N₂ and HCHO (10 ppm) + O₂ (20 v/v%). Fig. 6d and S15 illustrate that in the absence of O₂, peaks corresponding to DOM, formate, carbonate, CO₂, and H₂O are fainter than those with O₂, suggesting that O₂ is necessary for the entire oxidation process. Nevertheless, formate peaks at 1370 cm⁻¹ continue to increase over time, suggesting that the transformation of DOM to formate can proceed even in the absence of O₂. This implies that O₂ is not indispensable for DOM oxidation, and it is hypothesized that certain active oxygen species exist on Co single atoms, facilitating DOM transformation. Moreover, the

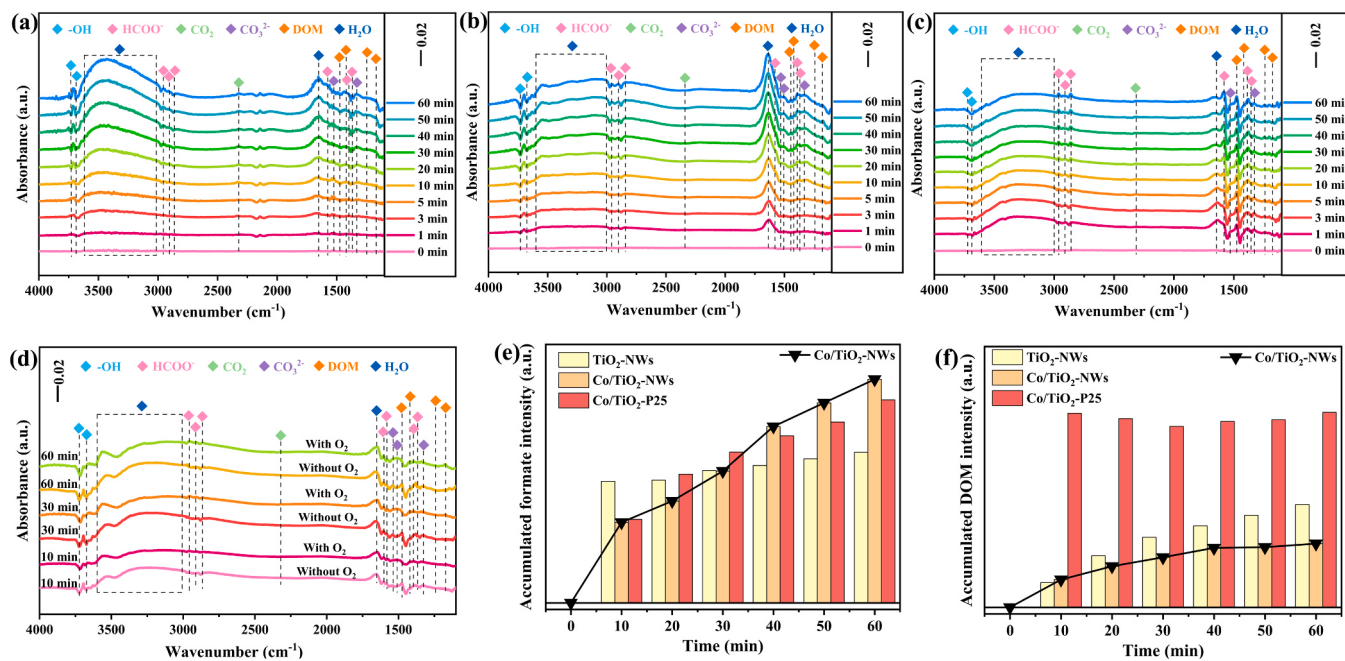


Fig. 6. In situ DRIFTS of (a) Co/TiO₂-NWs, (b) TiO₂-NWs, and (c) Co/TiO₂-P25 (Reaction conditions: 10 ppm HCHO, 50% RH, 20 v/v% O₂ and 30 °C), (d) In situ DRIFTS of Co/TiO₂-NWs in the presence and absence of O₂. Accumulated intensity of (e) formate and (f) DOM species.

formate peak increase coincides with decreasing peaks representing carbonate, confirming that the absence of O₂ inhibits formate-to-carbonate conversion but not formate formation. Thus, carbonate production appears to be highly dependent on the presence of gaseous O₂, and the reaction between formate and O₂ follows the Eley-Rideal mechanism [62]. Despite the inhibition of carbonate formation, the CO₂ peak appears, and the -OH peak intensity gradually diminishes. Consequently, surface -OH aids oxidation, promoting formate conversion to CO₂ in the absence of O₂.

Based on the DRIFTS results, we further conducted DFT calculations to simulate the degradation pathways of HCHO, particularly for the transformation of DOM to formate, to validate the promotional effect of Co single atoms on the catalytic oxidation of HCHO. Fig. 7a-c illustrate the sequential steps of HCHO oxidation for TiO₂-NWs, Co/TiO₂-P25, and Co/TiO₂-NWs, respectively. In Fig. 7a, the exposed (101) facet of anatase TiO₂ with a surface -OH group representing TiO₂-NWs was employed for HCHO oxidation. The unsaturated Ti_{5c} on the TiO₂(101) surface activates O₂, as depicted in step I-II. The adsorbed O₂ bound to Ti_{5c} is measured at an average distance of 2.07 Å with an adsorption energy of -1.10 eV in step I-II. The distance between the two oxygen atoms is 1.33 Å. This O₂ activation aligns with previous observations indicating that in the presence of subsurface oxygen vacancies in TiO₂(101), adsorbed O₂ can be effectively activated into O₂[·] at the top of Ti_{5c}, featuring a -1.0 eV adsorption energy and a 1.35 Å O=O length [63]. Thus, adsorbed O₂ is similarly activated into O₂[·] over TiO₂(101). In step III-IV, O₂[·] over TiO₂(101) exhibits weak oxidizability to oxidize HCHO into formate, demanding an exceedingly high energy barrier of 3.02 eV. TiO₂(101) shows limited activation due to inadequate electron transfer from Ti_{5c} to O₂, resulting in weak antibonding that fails to effectively separate the oxygen atoms. However, despite the high energy barrier, catalytic oxidation of HCHO can still occur on TiO₂, as observed in Figs. 5a-5c. In this reaction pathway, O₂ is actually activated not by Ti_{5c} but by surface oxygen vacancies. The rate-determining step involves the oxidation of DOM to formate by active oxygen atoms at oxygen vacancies, with a barrier energy of 2.67 eV (Fig. S16). Additional detailed information about the TiO₂ mechanism is provided in the Supplementary Material.

A CoO (Co₃₂O₃₂) slab in a 4 × 2 × 1 supercell exposed with a (200)

facet is constructed to represent the CoO nanoparticles supported on TiO₂-P25, as shown in Fig. 7b. In step I-II, gaseous O₂ is adsorbed at the Co_{3c} site, aligning parallel to the surface, releasing energy of 1.25 eV. The O₂-Co_{3c} distance (1.87 Å) is shorter than that over TiO₂ [63], and the O-O distance (1.37 Å) is longer compared to TiO₂(101). Consequently, in step III-IV, CoO effectively oxidizes adsorbed HCHO to DOM (-0.32 eV) using one active oxygen (O_s) of O₂, while the other oxygen forms a bridging oxygen between two Co atoms. In step IV-V, the DOM undergoes further oxidation to formate (-2.48 eV). However, the transformation of DOM into formate over CoO requires an activation energy of 1.65 eV. Subsequently, in step V-VI, gaseous O₂ aids the further oxidation of formate to carbonate, releasing 3.29 eV. Notably, formate oxidation requires no activation energy. Thus, the HCHO conversion efficiency for Co/TiO₂-P25 is notably higher than that of TiO₂. In step VI-VII, the carbonate further decomposes into CO₂, leaving one oxygen atom bound to Co/TiO₂-P25. This step requires an energy of 0.20 eV, suggesting that although slightly difficult, CO₂ can be generated from HCHO oxidation on Co/TiO₂-P25. Finally, O₂-Co/TiO₂-P25 is regenerated as the bridging oxygen connects with the residual oxygen to produce O₂. However, the final step (VII-VIII) demands a high energy of 1.39 eV, indicating difficulty in O₂ regeneration. Consequently, active sites for HCHO oxidation over Co/TiO₂-P25 are continuously depleted without adequate recovery, causing a gradual decrease in oxidation efficiency, as shown in Fig. 5a.

As shown in Fig. 7c, the adsorption of O₂ exhibits a much higher energy release of 3.14 eV than TiO₂(101) and CoO in step I-II, implying a stronger Co-O₂ bond. Furthermore, the adsorbed O₂ adopts a bidentate configuration with a 1.40 Å bond length, which is longer than that of CoO. Consequently, the Co single atom more effectively activates O₂. Accordingly, in step III-IV, adsorbed HCHO is strongly oxidized by one O_s of O₂ to generate DOM, releasing a higher energy of 0.96 eV than CoO. Subsequently, DOM converts to monodentate formate in step IV-V, with one hydrogen atom moving toward the aldehyde oxygen of HCHO, releasing an energy of 2.87 eV. Here, O_s bound to the carbon atom draws closer, reducing the bond length from 1.38 Å to 1.23 Å, signifying ongoing O_s oxidation of HCHO. This step demands an energy barrier of 0.74 eV, which is significantly lower than that of CoO. This suggests more thermodynamically and kinetically favored oxidation of

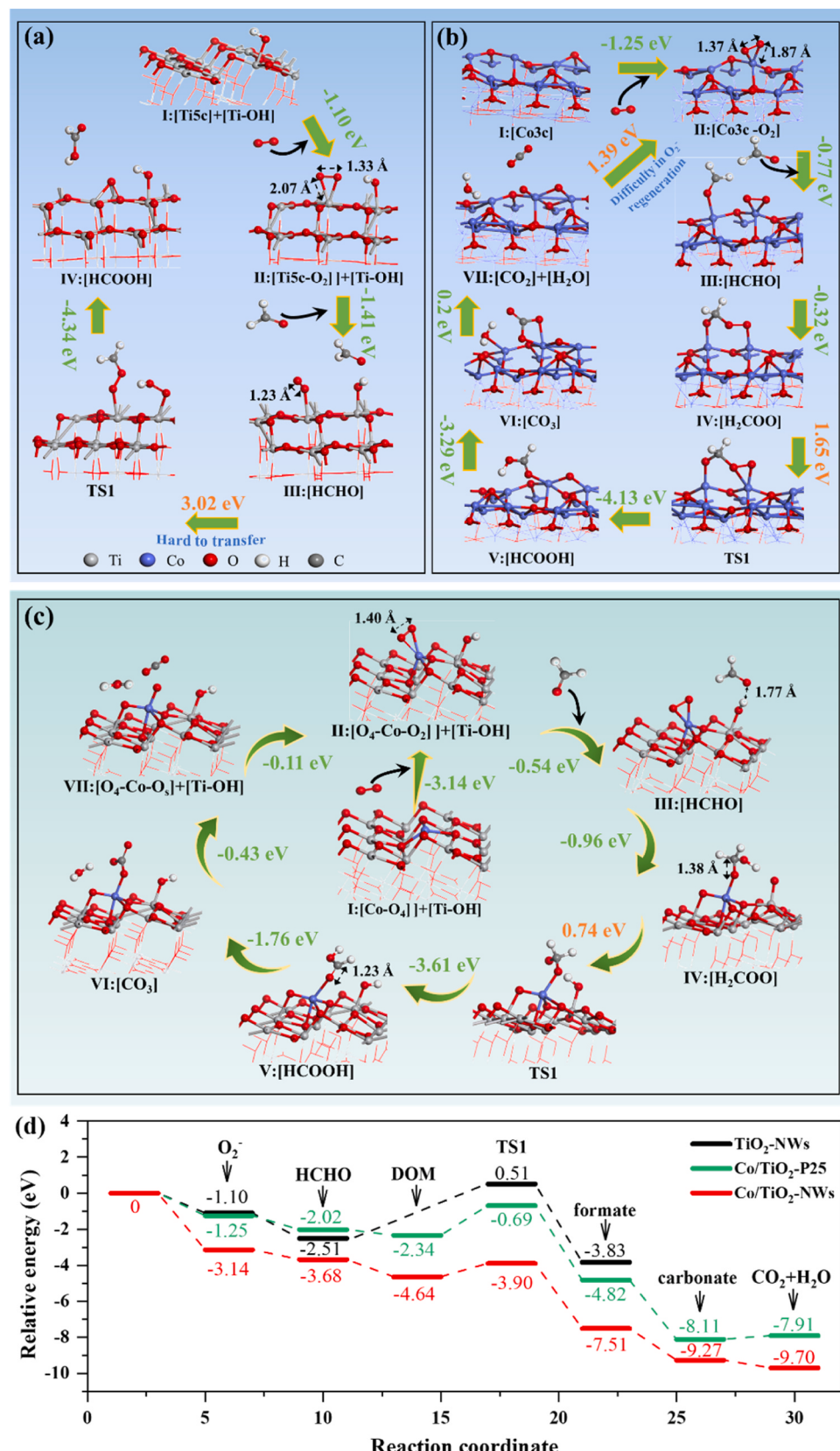


Fig. 7. Calculated energy profiles of HCHO oxidation on (a) TiO_2 -NWs, (b) Co/TiO_2 -P25, and (c) Co/TiO_2 -NWs, (d) relative-energy pathways of intermediate formation in HCHO catalytic oxidation on TiO_2 -NWs, Co/TiO_2 -P25, and Co/TiO_2 -NWs.

DOM over Co/TiO₂-NWs compared to Co/TiO₂-P25, although the reaction rate limitation still applies. In step V→VI, gaseous O₂ oxidizes formate into monodentate carbonate and H₂O with an exothermic energy of 1.76 eV. The transition state demands no energy barrier, as the carbonate's two oxygen atoms originate from gaseous O₂, and the oxygen of decomposed H₂O comes from HCHO. Finally, carbonate decomposes into CO₂, leaving O_s on the Co site binding with bridging oxygen to reform O₂. This transition also proceeds spontaneously without an energy barrier due to an energy-neutral state from carbonate decomposition (−0.43 eV) to O-Co_{bridging}-O breaking (0.28 eV). Overall, this reaction releases 6.56 eV with an energy barrier of 0.74 eV during DOM to formate transformation. Comparing the energy states among the three catalysts (Fig. 7d), we conclude that Co single atoms activate O₂ most effectively.

3.4. Excellent O₂-activation ability of Co single atoms

The aforementioned results show the crucial role of the reactive oxygen species generated by Co single atoms in HCHO oxidation. To gain insights into the underlying mechanism, we conducted further investigation to identify these active oxygen species.

Four distinct oxygen species — superoxide (O₂), monoatomic oxygen (O), surface lattice oxygen (O_L²⁻), and bulk lattice oxygen (O_L²⁻) [64], were distinguished among the four catalysts using O₂-TPD characterization. Their desorption temperature increases with their stability, as shown in Fig. 8a. Oxygen desorption peaks within the temperature ranges of 100–250 °C, 250–450 °C, 450–550 °C, and > 550 °C correspond to O₂[−], O[−], surface O_L²⁻, and bulk O_L²⁻, respectively [65,66]. Table S4 summarizes the concentration of oxygen species desorbed at different temperatures, with the integrated peak area normalized by catalyst weight. Notably, O₂ desorption peaks are present in Co/TiO₂-NWs (185.9 °C) and Co/TiO₂-P25 (182.9 °C), while they are not observed in TiO₂-NWs and TiO₂-P25. This slightly higher O₂ desorption temperature indicates a stronger binding of O₂ to Co single atoms compared to CoO nanoparticles, aligning with the DFT calculation results. Thus, more electrons were transferred from the Co single atom to the π^* orbitals, enhancing the O₂ activity [67]. Furthermore, Co/TiO₂-NWs exhibit a larger O₂ peak area than Co/TiO₂-P25, confirming that Co single atoms possess superior oxygen activation ability compared to CoO nanoparticles. The desorption peaks between 250–450 °C in all four catalysts are ascribed to O[−] resulting from O₂ dissociation within oxygen vacancies [68]. In addition, both Co/TiO₂-NWs and Co/TiO₂-P25 exhibit desorption peaks for surface O_L²⁻ and bulk O_L²⁻. Given the strong correlation between O₂ and HCHO catalytic performance among the four

catalysts, it is evident that O₂ is the predominant active oxygen species for HCHO oxidation.

In the FTIR analysis presented in Fig. 8b, noteworthy characteristic peaks of O₂ become prominent in Co/TiO₂-NWs and Co/TiO₂-P25 at 1012 and 1165 cm^{−1} upon Co loading. These peaks correspond to the O₂ bonding with Co(II) [56,69]. Notably, neither TiO₂-NWs nor TiO₂-P25 exhibits any O₂ peaks. Furthermore, the absorption intensity of the O₂ peak in Co/TiO₂-NWs is markedly higher than that in Co/TiO₂-P25. This result suggests that Co single atoms possess a superior ability to activate O₂ compared to CoO nanoparticles. Additionally, upon comparing the FTIR spectra before and after regeneration, as illustrated in Fig. S17, it becomes evident that the restoration of the Co/TiO₂-NWs activity can be attributed to the recovery of O₂.

To elucidate the exceptional O₂ activation capability of Co single atoms, we first computed the formation energy of Co single atoms to evaluate their activity. As shown in Fig. 9a, the formation energy of Co single atoms is −2.80 eV, substantially lower than −17.90 eV for a top Ti_{5c} within TiO₂(101) and −6.29 eV for a top Co_{3c} atom within CoO (200). This notably lowest formation energy indicates that the Co single atoms exhibit great reactivity compared to Co_{3c} and Ti_{5c}, endowing them with a higher potential for interacting with adsorbed O₂. Additionally, the structure arrangement of the Co single atom, encompassing its four neighboring O_{Ls}, exhibits a distorted D_{4h} symmetry. This configuration features b_{1g} (Co 3d_{xy}² and O 2p) and b_{2g} (Co 3d_{xy/xz/yz} and O 2p) symmetric bond orbitals that play a more significant role than the e_g (Co 3d_{z2} and O 2p) orbital in Co-O bonding. Consequently, the Co single atom possesses a conspicuously unoccupied d_{z2}² orbital, which boosts O₂ activation [70]. In contrast, the Ti_{5c} 3d_{z2}² and 3d_{xy/xz/yz} orbitals, serving as the primary bond orbitals for O₂ activation within an Oh symmetry, are largely occupied due to their involvement in connecting the adjacent O_{Ls}. Similarly, the Co_{3c} 3d_{xy/xz/yz} orbitals, characterized by T_d symmetry, are also engaged in bonding with O_{Ls}. Therefore, Co single atoms retain more unsaturated orbitals than those of Ti_{5c} and Co_{3c}, facilitating a more favorable interaction with adsorbed O₂. Subsequently, the Bader charge analysis in Fig. 9b indicates that individual oxygen atoms of adsorbed O₂ draw 0.437 and 0.418 e[−] from the Co single atom, a higher electron donation compared to Ti_{5c} (0.281 and 0.210 e[−]) and Co_{3c} (0.305 and 0.288 e[−]). These results confirm a substantial electron transfer from the Co single atom to the adsorbed O₂, leading to a valence state of −0.72 for the individual O, as opposed to the valence state of −2 exhibited by each O_L (−1.20 e[−]). Ultimately, this electron-enriched configuration of O_{2ads} on the Co single atom populates its antibonding π orbital, resulting in significantly enhanced oxidizability compared to Ti_{5c} and Co_{3c}.

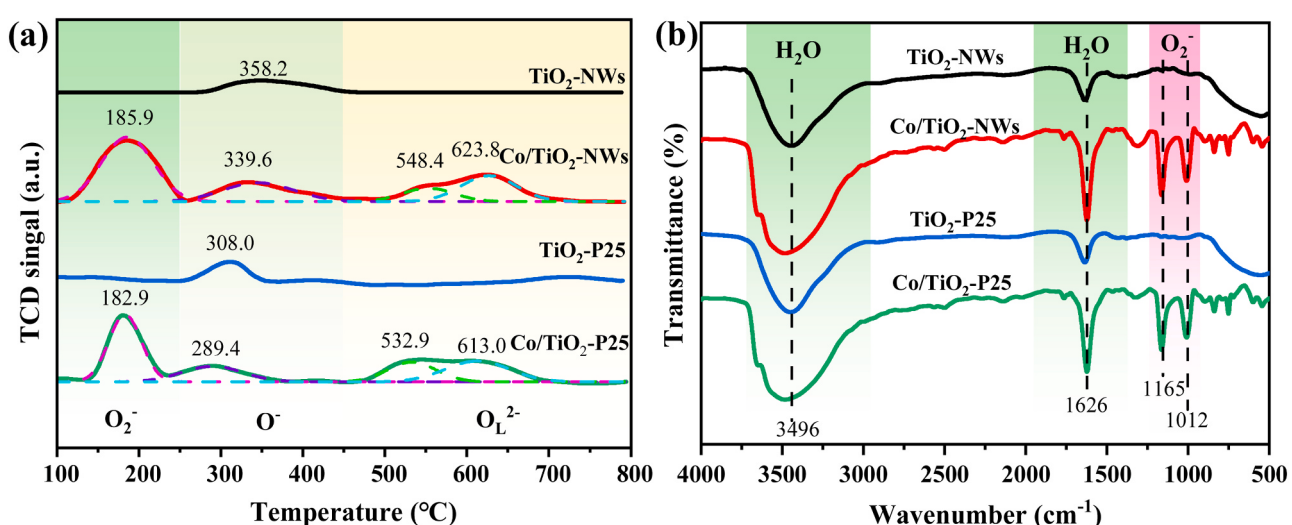


Fig. 8. (a) O₂-TPD spectra and (b) FTIR spectra of TiO₂-NWs, Co/TiO₂-NWs, TiO₂-P25, and Co/TiO₂-P25.

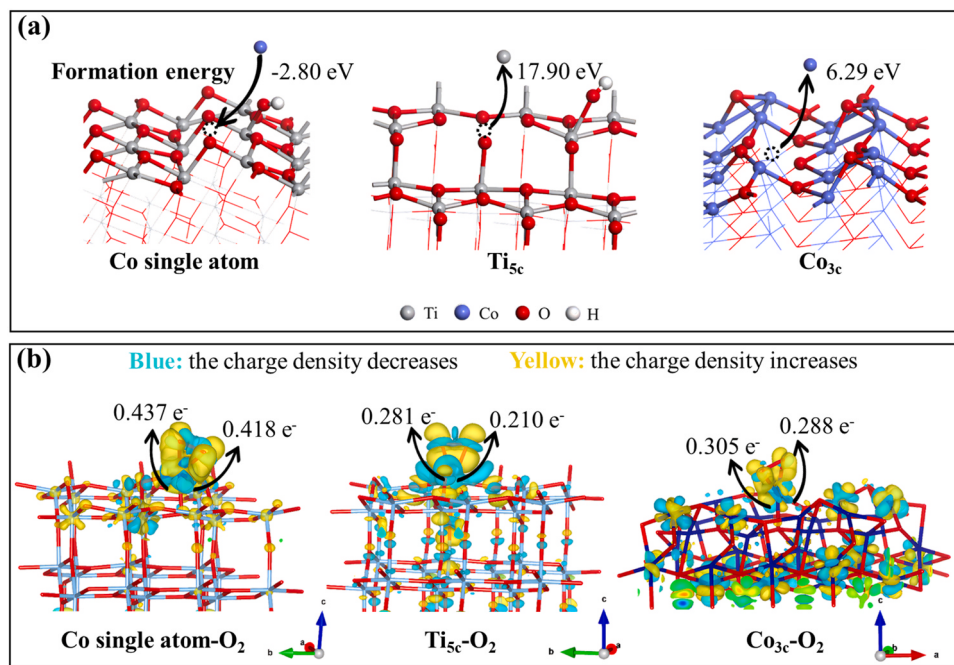


Fig. 9. (a) Formation energies of Co single atom, Ti_{5c} and Co_{3c}, respectively. (b) Bader charge analysis after adsorption of O₂ by Co/TiO₂-NWs, TiO₂-NWs, and Co/TiO₂-P25, respectively.

4. Conclusion

We successfully developed a monoatomic Co catalyst exhibiting exceptional oxygen activation capability, demonstrating remarkable efficiency and stable catalytic oxidation performance of HCHO at room temperature. The rate-limiting step of HCHO catalytic oxidation on TiO₂-NWs was the transformation from DOM to formate. The introduction of Co single atoms exhibited enhanced adsorption and activation ability for O₂, leading to the abundant generation of O₂, thereby reducing the energy barrier of the decisive step. The superior O₂ activation ability of the Co single atom can be attributed to its active nature and unsaturated electronic configuration.

CRediT authorship contribution statement

Shen Hua-zhen: Formal analysis, Funding acquisition, Supervision, Writing – review & editing. **Xia Wenjie:** Funding acquisition, Software, Supervision. **Liu Lijuan:** Conceptualization, Data curation, Investigation, Methodology, Writing – original draft. **Jing Guohua:** Formal analysis, Funding acquisition, Supervision. **Xu Cibin:** Investigation, Methodology. **Zhang Xiaowei:** Investigation, Methodology. **Zhang Xuehong:** Data curation, Investigation. **Guo Lingyun:** Investigation. **Huang Zhiwei:** Supervision, Methodology. **Wu Xiaomin:** Supervision. **Zhao Huawang:** Supervision. **Yuan Chung-Shin:** Supervision.

Declaration of Competing Interest

The authors declare that they have no known competing financial interests or personal relationships that could have appeared to influence the work reported in this paper.

Data Availability

Data will be made available on request.

Acknowledgment

This study was supported by the Fundamental Research Funds for the

Central Universities (ZQN-1016), and the National Natural Science Foundation of China (Grant No. 51908230). W. Xia gratefully acknowledges the support from the Department of Aerospace Engineering at Iowa State University. The authors are grateful for their financial support in order to accomplish this study. The supplemented materials have other 4 tables and 17 figures.

Appendix A. Supporting information

Supplementary data associated with this article can be found in the online version at doi:10.1016/j.apcatb.2023.123634.

References

- [1] A. Yusuf, C. Snape, J. He, H. Xu, C. Liu, M. Zhao, G.Z. Chen, B. Tang, C. Wang, J. Wang, S.N. Behera, Advances on transition metal oxides catalysts for formaldehyde oxidation: a review, *Cat. Rev.* 59 (2017) 189–233.
- [2] C.J. Na, M.J. Yoo, D.C.W. Tsang, H.W. Kim, K.H. Kim, High-performance materials for effective sorptive removal of formaldehyde in air, *J. Hazard. Mater.* 366 (2019) 452–465.
- [3] J. Yu, X. Li, Z. Xu, W. Xiao, NaOH-modified ceramic honeycomb with enhanced formaldehyde adsorption and removal performance, *Environ. Sci. Technol.* 47 (2013) 9928–9933.
- [4] M. Zhu, Y. Muhammad, P. Hu, B. Wang, Y. Wu, X. Sun, Z. Tong, Z. Zhao, Enhanced interfacial contact of dopamine bridged melamine-graphene/TiO₂ nano-capsules for efficient photocatalytic degradation of gaseous formaldehyde, *Appl. Catal. B: Environ.* 232 (2018) 182–193.
- [5] P. Fu, P. Zhang, J. Li, Photocatalytic degradation of low concentration formaldehyde and simultaneous elimination of ozone by-product using palladium modified TiO₂ films under UV254+185nm irradiation, *Appl. Catal. B: Environ.* 105 (2011) 220–228.
- [6] X. Zhu, X. Gao, R. Qin, Y. Zeng, R. Qu, C. Zheng, X. Tu, Plasma-catalytic removal of formaldehyde over Cu-Ce catalysts in a dielectric barrier discharge reactor, *Appl. Catal. B: Environ.* 170 (2015) 293–300.
- [7] R. Chen, Z. Sun, C. Hardacre, X. Tang, Z. Liu, The current status of research on the catalytic oxidation of formaldehyde, *Cat. Rev.* (2022) 1–56.
- [8] H. Zhang, G. Guo, Z. Wang, Q. He, X. He, H. Ji, Superior performance of formaldehyde complete oxidation at ambient temperature over Co single-atom catalysts, *Appl. Catal. B: Environ.* 333 (2023), 122774.
- [9] N. Li, B. Huang, X. Dong, J. Luo, Y. Wang, H. Wang, D. Miao, Y. Pan, F. Jiao, J. Xiao, Z. Qu, Bifunctional zeolites-silver catalyst enabled tandem oxidation of formaldehyde at low temperatures, *Nat. Commun.* 13 (2022), 2209.
- [10] Y. Zhuo, X. Guo, W. Cai, T. Shao, D. Xia, C. Li, S. Liu, Synergetic modulation of molecular oxygen activation and surface acidity/basicity on defective M/UiO-66m (M = Pt, Pd) for advanced oxidation of gaseous formaldehyde at room temperature, *Appl. Catal. B: Environ.* 333 (2023), 122789.

[11] Q. Liu, Y. Wang, M. Wen, Y. Guo, Y. Wei, G. Li, T. An, Catalytic oxidation of formaldehyde over a Au@Co₃O₄ nanocomposite catalyst enhanced by visible light: moisture indispensability and reaction mechanism, *Environ. Sci. Nano* 9 (2022) 4162–4176.

[12] D. Fang, J. Zheng, C. Han, W. Zhao, Y. Lu, B. Sun, L. Sun, X. Wang, H. Yan, Electro-injection-enhanced catalytic formaldehyde degradation based on conductive MnO_x cellulose aerogels at room temperature, *Appl. Catal. B: Environ.* 334 (2023), 122837.

[13] R. Long, K. Mao, X. Ye, W. Yan, Y. Huang, J. Wang, Y. Fu, X. Wang, X. Wu, Y. Xie, Y. Xiong, Surface facet of palladium nanocrystals: a key parameter to the activation of molecular oxygen for organic catalysis and cancer treatment, *J. Am. Chem. Soc.* 135 (2013) 3200–3207.

[14] M.M. Montemore, M.A. van Spronsen, R.J. Madix, C.M. Friend, O₂ activation by metal surfaces: implications for bonding and reactivity on heterogeneous catalysts, *Chem. Rev.* 118 (2018) 2816–2862.

[15] J. Ren, Y. Wang, J. Zhao, S. Tan, H. Petek, K atom promotion of O₂ chemisorption on Au(111) surface, *J. Am. Chem. Soc.* 141 (2019) 4438–4444.

[16] M. Huang, Y. Li, M. Li, J. Zhao, Y. Zhu, C. Wang, V.K. Sharma, Active site-directed tandem catalysis on single platinum nanoparticles for efficient and stable oxidation of formaldehyde at room temperature, *Environ. Sci. Technol.* 53 (2019) 3610–3619.

[17] D. Zhu, Y. Huang, R. Li, T. Huang, J. Cao, Z. Shen, S.C. Lee, Formaldehyde oxidation over Co@N-doped carbon at room temperature: tunable Co size and intensified surface electron density, *ACS Environ. Sci. Technol. Eng.* 1 (2021) 917–927.

[18] L. Yu, D. Deng, X. Bao, Chain mail for catalysts, *Angew. Chem. Int. Ed.* 59 (2020) 15294–15297.

[19] L. Yang, L. Shi, D. Wang, Y. Lv, D. Cao, Single-atom cobalt electrocatalysts for foldable solid-state Zn-air battery, *Nano Energy* 50 (2018) 691–698.

[20] X. Han, X. Ling, Y. Wang, T. Ma, C. Zhong, W. Hu, Y. Deng, Generation of nanoparticle, atomic-cluster, and single-atom cobalt catalysts from zeolitic imidazol frameworks by spatial isolation and their use in zinc-air batteries, *Angew. Chem. Int. Ed.* 58 (2019) 5359–5364.

[21] Z. Gao, W. Yang, X. Ding, G. Lv, W. Yan, Support effects on adsorption and catalytic activation of O₂ in single atom iron catalysts with graphene-based substrates, *Phys. Chem. Chem. Phys.* 20 (2018) 7333–7341.

[22] H. Luo, S. Tian, H. Liang, H. Wang, S. Gao, W. Dai, Oxidative cleavage and ammoxidation of organosulfur compounds via synergistic Co-N_x sites and Co nanoparticles catalysis, *Nat. Commun.* 14 (2023), 2981.

[23] Y. Xiong, W. Sun, Y. Han, P. Xin, X. Zheng, W. Yan, J. Dong, J. Zhang, D. Wang, Y. Li, Cobalt single atom site catalysts with ultrahigh metal loading for enhanced aerobic oxidation of ethylbenzene, *Nano Res* 14 (2021) 2418–2423.

[24] H. Qi, L. Zhang, J. Yang, Y. Su, G. Zeng, A. Wang, T. Zhang, Highly efficient Co single-atom catalyst for epoxidation of plant oils, *J. Chem. Phys.* 154 (2021), 131103.

[25] M. Aykol, C. Wolverton, Local environment dependent GGA+U method for accurate thermochemistry of transition metal compounds, *Phys. Rev. B* 90 (2014), 115105.

[26] H. Zhang, Q. An, Y. Su, X. Quan, S. Chen, Co₃O₄ with upshifted d-band center and enlarged specific surface area by single-atom Zr doping for enhanced PMS activation, *J. Hazard. Mater.* 448 (2023), 130987.

[27] C. Hsieh, W. Fan, W. Chen, J. Lin, Adsorption and visible-light-derived photocatalytic kinetics of organic dye on Co-doped titania nanotubes prepared by hydrothermal synthesis, *Sep. Purif. Technol.* 67 (2009) 312–318.

[28] Y. Lu, Y. Lin, D. Wang, L. Wang, T. Xie, T. Jiang, A high performance cobalt-doped ZnO visible light photocatalyst and its photogenerated charge transfer properties, *Nano Res* 4 (2011) 1144–1152.

[29] D. Montalvo, G. Corro, F. Bañuelos, O. Olivares-Xomel, P. Arellanes, U. Pal, Selective alcohols production through CO₂ photoreduction using Co₃O₄/TiO₂ photocatalyst exploiting synergistic interactions between Ti³⁺, Co²⁺ and Co³⁺, *Appl. Catal. B: Environ.* 330 (2023), 122652.

[30] S. Cai, L. Wang, S. Heng, H. Li, Y. Bai, D. Wang, Q. Wang, P. Zhang, C. He, Interaction of single-atom platinum-oxygen vacancy defects for the boosted photosplitting water H₂ evolution and CO₂ photoreduction: experimental and theoretical study, *J. Phys. Chem. C* 124 (2020) 24566–24579.

[31] J. Li, M. Zhang, Z. Guan, Q. Li, C. He, J. Yang, Synergistic effect of surface and bulk single-electron-trapped oxygen vacancy of TiO₂ in the photocatalytic reduction of CO₂, *Appl. Catal. B: Environ.* 206 (2017) 300–307.

[32] M. He, Y. Cao, J. Ji, K. Li, H. Huang, Superior catalytic performance of Pd-loaded oxygen-vacancy-rich TiO₂ for formaldehyde oxidation at room temperature, *J. Catal.* 396 (2021) 122–135.

[33] Z. Wang, E. Almatrafi, H. Wang, H. Qin, W. Wang, L. Du, S. Chen, G. Zeng, P. Xu, Cobalt single atoms anchored on oxygen-doped tubular carbon nitride for efficient peroxyxonoulfate activation: simultaneous coordination structure and morphology modulation, *Angew. Chem. Int. Ed.* 61 (2022), e202202338.

[34] N. Wang, K. Shen, L. Huang, X. Yu, W. Qian, W. Chu, Facile route for synthesizing ordered mesoporous Ni-Ce-Al oxide materials and their catalytic performance for methane dry reforming to hydrogen and syngas, *ACS Catal.* 3 (2013) 1638–1651.

[35] C.H. Park, S.B. Zhang, S. Wei, Origin of p-type doping difficulty in ZnO: the impurity perspective, *Phys. Rev. B* 66 (2002), 073202.

[36] S. Sun, X. Wu, Z. Huang, H. Shen, H. Zhao, G. Jing, Engineering stable Pt nanoclusters on defective two-dimensional TiO₂ nanosheets by introducing SMSI for efficient ambient formaldehyde oxidation, *Chem. Eng. J.* 435 (2022), 135035.

[37] B. McAllister, L.M. Liu, H.Q. Ye, P. Hu, Identifying an O₂ supply pathway in CO oxidation on Au/TiO₂(110): a density functional theory study on the intrinsic role of water, *J. Am. Chem. Soc.* 128 (2006) 4017–4022.

[38] C. Wang, K. Wang, Y. Feng, C. Li, X. Zhou, L. Gan, Y. Feng, H. Zhou, B. Zhang, X. Qu, H. Li, J. Li, A. Li, Y. Sun, S. Zhang, G. Yang, Y. Guo, S. Yang, T. Zhou, F. Dong, K. Zheng, L. Wang, J. Huang, Z. Zhang, X. Han, Co and Pt dual-single-atoms with oxygen-coordinated Co-O-Pt dimer sites for ultrahigh photocatalytic hydrogen evolution efficiency, *Adv. Mater.* 33 (2021), 2003327.

[39] J. Long, Z. Yan, Y. Gong, J. Lin, MOF-derived Cl/O-doped C/CoO and C nanoparticles for high performance supercapacitor, *Appl. Surf. Sci.* 448 (2018) 50–63.

[40] C. Liu, J. Qian, Y. Ye, H. Zhou, C. Sun, C. Sheehan, Z. Zhang, G. Wan, Y.-S. Liu, J. Guo, S. Li, H. Shin, S. Hwang, T.B. Gunnoe, W.A. Goddard, S. Zhang, Oxygen evolution reaction over catalytic single-site Co in a well-defined brookite TiO₂ nanorod surface, *Nat. Catal.* 4 (2020) 36–45.

[41] Z. Zhang, X. Zhao, S. Xi, L. Zhang, Z. Chen, Z. Zeng, M. Huang, H. Yang, B. Liu, S. J. Pennycook, P. Chen, Atomically dispersed cobalt trifunctional electrocatalysts with tailored coordination environment for flexible rechargeable Zn-Air battery and self-driven water splitting, *Adv. Energy Mater.* 10 (2020), 2002896.

[42] Y. Chen, R. Gao, S. Ji, H. Li, K. Tang, P. Jiang, H. Hu, Z. Zhang, H. Hao, Q. Qu, X. Liang, W. Chen, J. Dong, D. Wang, Y. Li, Atomic-level modulation of electronic density at cobalt single-atom sites derived from metal-organic frameworks: enhanced oxygen reduction performance, *Angew. Chem. Int. Ed.* 60 (2021) 3212–3221.

[43] X. Wu, S. Sun, R. Wang, Z. Huang, H. Shen, H. Zhao, G. Jing, Pt single atoms and defect engineering of TiO₂-nanosheet-assembled hierarchical spheres for efficient room-temperature HCHO oxidation, *J. Hazard. Mater.* 454 (2023), 131434.

[44] S.B. Do, S.E. Lee, T.O. Kim, Oxidative decomposition with PEG-MnO₂ catalyst for removal of formaldehyde: Chemical aspects on HCHO oxidation mechanism, *Appl. Surf. Sci.* 598 (2022), 153773.

[45] S. Rong, K. Li, P. Zhang, F. Liu, J. Zhang, Potassium associated manganese vacancy in birnessite-type manganese dioxide for airborne formaldehyde oxidation, *Catal. Sci. Technol.* 8 (2018) 1799–1812.

[46] L. Zhang, Q. Bao, B. Zhang, Y. Zhang, S. Wan, S. Wang, J. Lin, H. Xiong, D. Mei, Y. Wang, Distinct role of surface hydroxyls in single-atom Pt₁/CeO₂ catalyst for room-temperature formaldehyde oxidation: acid-base versus redox, *J. Am. Chem. Soc.* Au 2 (2022) 1651–1660.

[47] Y. Li, B. Xu, Y. Fan, N. Feng, A. Qiu, J.M.J. He, H. Yang, Y. Chen, The effect of titania polymorph on the strong metal-support interaction of Pd/TiO₂ catalysts and their application in the liquid phase selective hydrogenation of long chain alkadienes, *J. Mol. Catal. A Chem.* 216 (2004) 107–114.

[48] Y. Huo, X. Wang, Z. Rui, X. Yang, H. Ji, Identification of the nearby hydroxyls' role in promoting HCHO oxidation over a Pt catalyst, *Ind. Eng. Chem. Res.* 57 (2018) 8183–8189.

[49] K. Vikrant, K.H. Kim, C. He, D.A. Giannakoudakis, Harnessing adsorption-catalysis synergy: efficient oxidative removal of gaseous formaldehyde by a manganese dioxide/metal-organic framework nanocomposite at room temperature, *Adv. Funct. Mater.* 32 (2022), 2107922.

[50] J. Ye, M. Zhou, Y. Le, B. Cheng, J. Yu, Three-dimensional carbon foam supported MnO₂/Pt for rapid capture and catalytic oxidation of formaldehyde at room temperature, *Appl. Catal. B: Environ.* 267 (2020), 118689.

[51] S. Zhang, Y. Zhuo, C.I. Ezugwu, C. Wang, C. Li, S. Liu, Synergistic molecular oxygen activation and catalytic oxidation of formaldehyde over defective MIL-88B(Fe) nanorods at room temperature, *Environ. Sci. Technol.* 55 (2021) 8341–8350.

[52] C. Ma, S. Sun, H. Lu, Z. Hao, C. Yang, B. Wang, C. Chen, M. Song, Remarkable MnO₂ structure-dependent H₂O promoting effect in HCHO oxidation at room temperature, *J. Hazard. Mater.* 414 (2021), 125542.

[53] J. Yang, H. Yang, M. Niu, H. Zhou, X. Yi, D. Chang, J. Zhan, Y. Liu, Ultra-light 3D MnO₂-agar network with high and longevous performance for catalytic formaldehyde oxidation, *Sci. Total Environ.* 830 (2022), 154818.

[54] C. Zhang, F. Liu, Y. Zhai, H. Ariga, N. Yi, Y. Liu, K. Asakura, M. Flytzani-Stephanopoulos, H. He, Alkali-metal-promoted Pt/TiO₂ opens a more efficient pathway to formaldehyde oxidation at ambient temperatures, *Angew. Chem. Int. Ed.* 51 (2012) 9628–9632.

[55] S. Rong, T. He, P. Zhang, Self-assembly of MnO₂ nanostructures into high purity three-dimensional framework for high efficiency formaldehyde mineralization, *Appl. Catal. B: Environ.* 267 (2020), 118375.

[56] F. Liu, X. Liu, J. Shen, A. Bahi, S. Zhang, L. Wan, F. Ko, The role of oxygen vacancies on Pt/NaInO₂ catalyst in improving formaldehyde oxidation at ambient condition, *Chem. Eng. J.* 395 (2020), 125131.

[57] K. Zha, W. Sun, Z. Huang, H. Xu, W. Shen, Insights into high-performance monolith catalysts of Co₃O₄ nanowires grown on nickel foam with abundant oxygen vacancies for formaldehyde oxidation, *ACS Catal.* 10 (2020) 12127–12138.

[58] Y. Wang, K. Liu, J. Wu, Z. Hu, L. Huang, J. Zhou, T. Ishihara, L. Guo, Unveiling the effects of alkali metal ions intercalated in layered MnO₂ for formaldehyde catalytic oxidation, *ACS Catal.* 10 (2020) 10021–10031.

[59] R. Li, Y. Huang, D. Zhu, W. Ho, J. Cao, S. Lee, Improved oxygen activation over a carbon/Co₃O₄ nanocomposite for efficient catalytic oxidation of formaldehyde at room temperature, *Environ. Sci. Technol.* 55 (2021) 4054–4063.

[60] Z. Yan, Z. Xu, L. Yue, L. Shi, L. Huang, Hierarchical Ni-Al hydrotalcite supported Pt catalyst for efficient catalytic oxidation of formaldehyde at room temperature, *Chin. J. Catal.* 39 (2018) 1919–1928.

[61] X. Sun, J. Lin, Y. Wang, L. Li, X. Pan, Y. Su, X. Wang, Catalytically active IrO species supported on Al₂O₃ for complete oxidation of formaldehyde at ambient temperature, *Appl. Catal. B: Environ.* 268 (2020) 575–584.

[62] Y. Bu, Y. Chen, G. Jiang, X. Hou, S. Li, Z. Zhang, Understanding of Au-CeO₂ interface and its role in catalytic oxidation of formaldehyde, *Appl. Catal. B: Environ.* 260 (2020), 118138.

[63] U. Aschauer, J. Chen, A. Selloni, Peroxide and superoxide states of adsorbed O₂ on anatase TiO₂ (101) with subsurface defects, *Phys. Chem. Chem. Phys.* 12 (2010) 12956–12960.

[64] W. Song, A.S. Poyraz, Y. Meng, Z. Ren, S.-Y. Chen, S.L. Suib, Mesoporous Co₃O₄ with controlled porosity: inverse micelle synthesis and high-performance catalytic CO oxidation at -60 °C, *Chem. Mater.* 26 (2014) 4629–4639.

[65] J. Chen, M. Huang, W. Chen, H. Tang, Y. Jiao, J. Zhang, G. Wang, R. Wang, Defect engineering and synergistic effect in CoO catalyst for efficient removal of formaldehyde at room temperature, *Ind. Eng. Chem. Res.* 59 (2020) 18781–18789.

[66] H.P. Uppara, S.K. Singh, N.K. Labhsetwar, M.S. Murari, H. Dasari, The catalytic activity of Ce-Hf, Ce-Hf-Mg mixed oxides and RuO₂/HfO₂ deposited on CeO₂: role of superoxide/peroxide in soot oxidation reaction, *Korean J. Chem. Eng.* 38 (2021) 1403–1415.

[67] Y. Wang, J. Dai, M. Wang, F. Qi, X. Jin, L. Zhang, Enhanced toluene oxidation by photothermal synergistic catalysis on manganese oxide embedded with Pt single-atoms, *J. Colloid Interface Sci.* 636 (2023) 577–587.

[68] J. Yang, S. Hu, Y. Fang, S. Hoang, L. Li, W. Yang, Z. Liang, J. Wu, J. Hu, W. Xiao, C. Pan, Z. Luo, J. Ding, L. Zhang, Yan Guo, Oxygen vacancy promoted O₂ activation over perovskite oxide for low-temperature CO oxidation, *ACS Catal.* 9 (2019) 9751–9763.

[69] Y. Gong, M. Zhou, Spectroscopic and theoretical studies of transition metal oxides and dioxygen complexes, *Chem. Rev.* 109 (2009) 6765–6808.

[70] Y. Sun, S. Sun, H. Yang, S. Xi, J. Gracia, Z. Xu, Spin-related electron transfer and orbital interactions in oxygen electrocatalysis, *Adv. Mater.* 32 (2020), e2003297.

Further reading

[1] E.L. Hult, H. Willem, P.N. Price, T. Hotchi, M.L. Russell, B.C. Singer, Formaldehyde and acetaldehyde exposure mitigation in US residences: in-home measurements of ventilation control and source control, *Indoor Air* 25 (2015) 523–535.